Effect of RuO_xH_y Island Size on PtRu Particle Aging in Methanol

Badri Shyam,[†] Thomas M. Arruda,[‡] Sanjeev Mukerjee,[‡] and David E. Ramaker*[,†]

Department of Chemistry, The George Washington University, Washington, D.C. 20052, and Department of Chemistry and Chemical Biology, Northeastern University, Boston, Massachusetts 02115

Received: June 8, 2009; Revised Manuscript Received: September 4, 2009

The aging properties of two different commercial PtRu black catalysts, Johnson-Matthey HiSpec6000 and Tanaka TEC90110, were observed in 1 M trifluoromethanesulfonic acid with 0.3 M methanol as a function of both time and potential cycling. Cu underpotential deposition, cyclic voltammetry, and x-ray absorption spectroscopy, using both the extended x-ray absorption fine structure and $\Delta\mu$ x-ray absorption near-edge spectroscopy analysis techniques, on samples after potential cycling between 0.02 and 0.8 V, revealed the PtRu aging mechanism and offer an explanation of why the two catalysts age differently. The Tanaka catalyst had relatively large RuO_xH_y islands on the surface and underwent little dissolution and agglomeration after 40 cycles. This had little detrimental effect on the CO oxidation properties as seen in the CO stripping data, and therefore, this catalyst can be expected to be relatively more tolerant to poisoning in direct methanol fuel cells. The Johnson-Matthey catalyst, on the other hand, was found to have much smaller Ru islands initially, underwent more Ru dissolution/agglomeration, and showed definite signs of an increase in Ru island size and partial oxidation to RuO_xH_y. The CO stripping data for this catalyst show a significant increase in onset potential with aging, reflecting a change from the predominant bifunctional to ligand-effect mechanism for the CO oxidation.

1. Introduction

The cost, performance levels, vulnerability to poisoning, and durability of Pt-based proton exchange membrane (PEM) fuel cells have each in part kept them from large-scale commercialization. Earlier efforts concentrated on cost and performance levels, but as the particle size and loading of modern electrocatalysts have decreased to meet the first two issues, and bimetallics have been introduced to meet the third issue, the emphasis has turned to the durability of the bimetallic particles. The degradation with time of a PEM fuel cell involves both the membrane (e.g., Nafion) and the PtM (M = Ru, Co, Ni, Cr, Mo, etc.) electrocatalysts, but of these the most studied are the long-term changes to the electrocatalysts.[1] The degradation of the catalyst, resulting in current decay over time (i.e., in chronoamperometry experiments), can involve surface M atom rearrangements, particle growth, and/or M and Pt atom dissolution at the anode and cathode. Both Pt dissolution and agglomeration from pure Pt anodes and cathodes[2−14] have been extensively studied as well as the slow dissolution of Rh, Ru, or Sn from supported PtM bimetallic particles[15−22] in acid media during voltammetric cycling or fuel cell aging. While it is well-known that cathodic losses due to sluggish oxygen reduction reaction (ORR) kinetics are much more significant than anodic overpotential losses, in the case of the direct methanol fuel cell (DMFC) where methanol is oxidized on the PtRu surface, recent findings[23−25] reveal that the two processes are linked. The above-mentioned reports illustrated the degradation of the anode can eventually result in the rapid deterioration of cathode performance, drastically reducing the overall efficiency of the fuel cell. For example, in these PtRu catalysts, significant Ru dissolution from the anode has been observed and the leached Ru ions were found not only in the polymer electrolyte membrane, but also deposited on the surface of the Pt cathode. Cyclic voltammograms of the anode and cathode in the above-mentioned situation clearly indicate that the DMFC cathode becomes more anode-like and quickly leads to a steep loss in operating potential. Thus, it is of considerable interest to understand the processes of catalyst aging and degradation, not only from a fundamental standpoint but also with the aim of eliminating the various bottlenecks which keep such catalysts from widespread use in fuel cells.

A broad array of electrochemical, microscopic, and spectroscopic techniques have previously been used to study these aging effects. The mass loss from the anode/cathode has been observed directly using an electrochemical quartz crystal microbalance (EQCM)[26,27] as well as the presence of Pt or M atoms in the electrolyte using energy-dispersive x-ray (EDX) analysis.[18] Atom rearrangements or particle growth has been observed with atomic force microscopy (AFM),[7] x-ray diffraction (XRD),[2,4,18,19,21] scanning electron microscopy (SEM), transmission electron microscopy (TEM),[2,4,7,14,19,20] and x-ray absorption spectroscopy (XAS).[17,18,28]

The general mechanism for metal dissolution has been attributed to oxidation/reduction of the surface atoms, causing atom rearrangement and dissolution into the electrolyte[29,30] and sometimes even (both Pt and Ru) crossover from the anode to the cathode.[4,14,25,28] Detailed mechanistic information and kinetic models have been presented to characterize the particle agglomeration and atom dissolution.[29,30] Despite these numerous efforts and proposed models, many questions and issues remain regarding the relative rates of agglomeration and dissolution at the anode and cathode and their dependence on potential, particle loading, and morphology. A very important question, for example, is how the M atom dissolution depends on the RuO_xH_y island size on the surface. This question has not been considered,

* To whom correspondence should be addressed. Phone: (202) 994-6934. Fax: (202) 994-5873. E-mail: ramaker@gwu.edu.
[†] The George Washington University.
[‡] Northeastern University.

10.1021/jp905383n CCC: $40.75
Published on Web 10/15/2009

as generally the island size is unknown. Measuring the island size however is no trivial task. Very few methods are available to do such measurements in situ where it must be done as ex situ samples are known to be almost always fully oxidized.

As mentioned above, Ru dissolution from PtRu electrocatalysts during cycling in acid media with methanol present has been reported previously.[17] Holstein and Rosenfeld observed Ru dissolution when the catalyst was cycled over a large window (0−1.3 V vs RHE), while little or no dissolution was observed over much narrower potential ranges. Further, the dissolution was observed with catalysts loadings of ∼1/10 of those typically used in a DMFC and subsequently at much lower current densities. Chen et al.[16] established that the anode potential under normal operation in a DMFC was benign for the PtRu/C electrocatalyst, but in the case of deep discharge or a short circuit, the anode potential value could exceed 0.6 V, which apparently was detrimental to the catalyst. Recent studies by Wang and co-workers[31,32] using XPS, XRD, and electrochemical methods on PtRu catalysts have shown that while Pt is relatively stable, the Ru atoms undergo substantial oxidation. This oxidative process suggests the existence of these oxides/hydroxides of Ru may actually hinder the dissolution and agglomeration of Pt in the catalysts, thus slowing the aging/degradation process in these alloy catalysts. We suspect this conclusion may be highly dependent on the Ru island size. Others[25] have observed decay of the current with time even under normal operation. Thus, it has not yet been fully established exactly which potential ranges are required to see significant Pt or Ru dissolution/agglomeration and what the effects of Ru island size might be on this dissolution process. Recently it has been reported that covering the Pt particles with a monolayer of Au significantly slows the Pt dissolution process at nearly all potentials.[33]

In this work, electrochemistry and XAS were used to study the aging of two commercially available catalysts. In most XAS studies on alloys, the analysis chiefly involves studying the extended x-ray absorption fine structure (EXAFS) region to obtain changes in coordination numbers and bond lengths as a function of some electrochemical treatment. Here, in addition to conventional XAS analysis, the recently developed $\Delta\mu$-XANES (x-ray absorption near-edge structure) technique is used to observe small changes occurring on the surface of the catalysts.[34] The primary scope of this work is to examine Ru and Pt dissolution/agglomeration of PtRu black under conditions quite similar to those in a fuel cell, with n (0, 20, and 40) potential-sweep cycles between 0.02 and 0.8 V. Two different commercial PtRu catalysts (Johnson-Matthey (JM) and Tanaka) were utilized in 1 M trifluoromethanesulfonic acid (TFMSA) with 0.3 M methanol (MeOH) and their properties compared. Shown in Figure 1 are CO stripping curves for the two catalysts before and after the 8 h chronoamperometry (CA) session at 500 mV. The data were collected at a scan rate of 10 mV s^{-1}. In the case of the JM sample, there is a shift in the onset potential for the CO stripping, while there is no such shift for the Tanaka sample. Further, a positive shift in the peak potential of ca. 50 mV is observed in both catalyst samples. It is clear that the two catalysts exhibit different aging characteristics. To explain this difference in behavior, in situ XAS data were obtained on the samples and their change with cycling was observed using the $\Delta\mu$-XANES and EXAFS analysis techniques. It will be shown that the sensitivity of the $\Delta\mu$-XANES technique indeed allows changes in the particles to be observed in this potential range even after as few as 10−20 cycles.

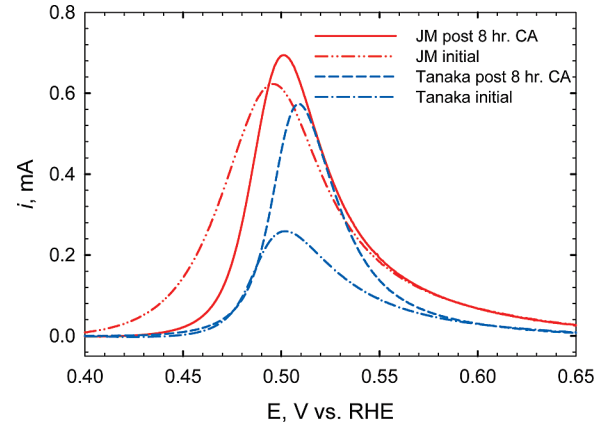

Figure 1. CO stripping data[24] for the Johnson-Matthey (red) and Tanaka (blue) catalysts before and after an 8 h chronoamperometic test at 500 mV. The data have not been normalized for surface area.

2. Experimental Methods and Data Analysis

2.1. Electrode Preparation and XAS Cell Assembly. Two different commercial PtRu (approximately 1:1 atomic ratio) based electrocatalysts were used for preparation of the working electrodes, the first obtained from Johnson-Matthey (HiSpec6000) and the second from Tanaka (TEC90110) (hereafter referred to as JM and Tanaka). The working electrodes were prepared in-house with a metal loading of 4.7 and 9.3 mg/cm^2 of Pt and Ru, respectively, by hand painting the inks (preweighed catalyst powder, deionized H_2O, and 5 wt % Nafion) onto carbon cloth (PANEX 30, Zoltek Corp.) by a standard method described previously.[35] The total geometric area of the electrodes was 5 cm^2. The metal loading was chosen on the basis of absorption cross sections for Pt and Ru to ensure an XAS step height of close to unity. The in situ XAS cells used were similar to a previously reported design[36] and were assembled by placing a Nafion 112 membrane between the PtRu working electrode and a Grafoil (GrafTech International) counter electrode. In all cells the current collectors used were 0.5 mm Au wires (99.999%, Alfa Aesar) and were mechanically pressed to the rear of each electrode in a location that did not impinge the X-ray beam path in the photon window. The cells were sealed using silicone gaskets (Auburn Chemical Co.). The electrolyte used in these experiments was 1 M TFMSA (triply distilled, Strem Chemicals) with the addition of 0.3 M methanol. An Autolab PGSTAT 30 potentiostat/galvanostat (Metrohm USA, formerly Brinkmann Instruments) was employed for potential control in all experiments.

2.2. In Situ XAS Measurements. No catalyst pretreatment (i.e., potential cycling) was performed prior to XAS measurements aside from soaking the working electrodes in electrolyte under vacuum for 1 h prior to experiment for the purpose of wetting. Full-range EXAFS scans were collected (−200 eV below the edge to k = 18 $Å^{-1}$ above the edge) at the Pt L_{III} edge (11564 eV) as well as the Ru K edge (22117 eV). A summary of the data collected is presented in Figure 2. Briefly, data were collected at both edges at the indicated potentials after 0, 20, and 40 cycles. In each case, all the data at a given edge were first collected in 1 M TFMSA and then with the addition of 0.3 M methanol, wherein a fresh electrode from the same batch of catalyst was used. In all, four electrodes were used for each catalyst to perform the designated experiments (with and without methanol at the Pt and Ru edges). Measurements were performed at beamline X23-A2 at the National Synchrotron Light Source (Brookhaven National Laboratory, Upton, NY), which employs a piezo-feedback-stabilized Si(311) monochro-

Catalysts	JM & Tanaka				
Electrolyte	1M TFMSA Clean, reference		1M TFMSA + 0.3M CH_3OH		
Cycles	0		20		40
Pot. (V, RHE)	0	0.24	0.54	0.70	0.84
Edges	Pt L_{III}		Ru K		

Figure 2. Summary of XAS data collected.

mator. XAS data were collected in transmission mode with the cell placed between two gas ionization chambers (I_0, incident beam intensity; I_1, transmitted beam intensity) and a Pt foil/Ru powder (325 mesh, Alfa Aesar) between I_1 and I_2 (beam intensity for the reference sample). The Pt and Ru reference foil scans were used to correct for any drift in the beam energy during data collection.

2.3. Electrochemical Measurements. All electrochemical measurements were carried out using 1 M TFMSA (Strem Chemicals), which was triply distilled by a method described elsewhere.[37] For surface area determination, aqueous solutions of 2 mM $CuSO_4$ (Alfa Aesar) were prepared in 1 M TFMSA and employed by the method outlined by Green et al.[38,39] Catalyst suspensions were produced by mixing a preweighed quantity of Pt, PtRu or Ru/C, deionized H_2O (18.2 MΩ, Millipore Milli-Q), and 5 wt % Nafion solution (suspended in low molecular weight alcohols, LQ-1105, Ion Power Inc.). The suspensions were sonicated for 15 min, stirred for 2 h, and then deposited onto a 9 mm polycrystalline Au slug. The total electrocatalyst target loading was 100 $\mu g \cdot cm^{-2}$, although some of the loosely bound particles may have washed off the surface prior to testing. The Au slug was connected to a threaded 316 stainless steel current-collecting rod which never contacted the electrolyte. The cells were comprised of a jacketed 50 cm^{-3} glass beaker with a machined PTFE lid. In all cases a sealed glass reference hydrogen electrode (RHE; 1 M TFMSA internal) was used and connected to the cell via a glass capillary which terminated at a fine porous frit to minimize Cu^{2+}, MeOH, and Ru^{n+} crossing into the RHE. The counter electrode was a Pt wire (Alfa Aesar, 99.999%) with a surface area of 1.7 cm^2 as determined by integrating the H_{upd}. The Ru surface area was determined by immersing the slug into a solution of Ar-purged (UHP, Middlesex Gasses) 1 M TFMSA + 2 mM $CuSO_4$ and polarizing to 0.3 V for 60 s. Subsequently, the potential was scanned anodically to 0.8 V. The Pt surface area measurement was carried out the same way except a starting potential of 0.4 V (also for 60 s) was used as Cu^{2+} will only deposit on Pt when potentiostatically controlled in that region. The electrode was then removed from the Cu^{2+}-containing electrolyte, rinsed with deionized H_2O, and placed into an identical cell containing clean 1 M TFMSA. A total of 500 cyclic voltammograms (CVs) were collected at a sweep rate of 50 mV s^{-1} between 0.02 and 0.8 V vs. RHE. Following the 500 cycles, surface area determinations were repeated by the procedure outlined above to illustrate any loss of electrocatalyst as a result of cycling. CO stripping voltammograms were collected by saturating the 1 M TFMSA with gaseous CO (5.0 grade, Middlesex Gasses) and scanning the potential anodically at a sweep rate of 10 mV s^{-1}.

2.4. XANES and EXAFS Analysis. Analysis of the XANES region of the XAS data was carried out using the $\Delta\mu$ technique[34,40−43] previously applied to adsorption of H, O/OH, and Cl on Pt[44−46] and PtM (M = Cr, Fe, Co, and Ni) cathodes[47] and PtRu anodes[48] in an electrochemical cell and even to Pt and PtRu anodes in an operating direct methanol fuel cell.[27] A brief summary is given here for clarity and to highlight slight differences from the previous methods.

All XAS data were processed using the ATHENA code developed by Ravel and Newville.[49] The pre-edge background is removed using the AUTOBK algorithm, described completely elsewhere,[50] followed by normalization over the 50−150 eV (relative to E_0) range for XANES analysis. This procedure was carried out for both the sample data in transmission mode ($\ln(I_0/I)$) and the reference foil data ($\ln(I/I_{ref})$). The foil data were then calibrated and aligned to the theoretical edge energy, and the resultant energy differences were transferred to the sample data; i.e., the ΔE shift determined for the foil at any given potential is added to the energy of the sample data at the same potential. This energy calibration corrects for shifts due to photon beam drift. This energy calibration is crucial for the success of the $\Delta\mu$ technique to ensure full cancellation of the atomic contribution in the XANES, which dominates the spectrum; the resulting $\Delta\mu$-XANES signal intensity is typically only about 1−5% of the total μ signal.

The difference $\Delta\mu = \mu(V) - \mu(V_{ref})$ is generally determined by subtracting the μ-XANES at an appropriate reference potential V_{ref} from μ-XANES at other potentials to highlight the effect of adsorbates. The reference potential V_{ref} is usually taken to be the potential at which the electrode is relatively free of adsorbates. However, the optimal choice of reference can change on the basis of the nature of the inquiry, the sample, the absorption edge, and the operating conditions. In this work, the electrode in 1 M TFMSA *without* methanol was used as the reference at 0.54 V at the Pt edge (when the Pt is relatively free of both H and O) and at 0.02 V at the Ru K edge (when the Ru is mostly free of O_x) with no cycling. Therefore, the $\Delta\mu$ signals (the notation used is the potential followed by the number of cycles) were obtained from the following differences:

$$\Delta\mu(V\_\text{cycles}) = \mu(V\_\text{cycles, MeOH}) - \mu(0.54\_0\text{, no MeOH}) \quad \text{for Pt} \quad (1)$$

$$\Delta\mu(V\_\text{cycles}) = \mu(V\_\text{cycles, MeOH}) - \mu(0.02\_0\text{, no MeOH}) \quad \text{for Ru} \quad (2)$$

As will be shown in Figure 7, CO and O(H) were visible as different features by this method, allowing for simultaneous indications of their coverages. The final $\Delta\mu$ curves were background corrected (80 eV smooth) and smoothed to remove random noise (5 eV) using a standard Savitzky−Golay smoothing routine with the indicated energy range given in parentheses.

The EXAFS fitting analyses were performed using the ARTEMIS code,[49] by employing only two first-shell metal atom scattering paths for each sample (either Pt−Pt and Pt−Ru or Ru−Ru and Ru−Pt) included at each edge. All fits were carried out on k^2 weighted $\chi(k)$ data using a Kaiser−Bessel window over a k range of 1.574 $Å^{-1} < k <$ 13.769 $Å^{-1}$ and an R window of 1.448 Å $< R <$ 3.201 Å. Details of the method for extracting coordination numbers (CNs) have been described elsewhere.[48] Several fits were first carried out on the data obtained, allowing all four parameters per path (N, R, σ, and E_0) to vary. It was found that σ^2 (the Debye−Waller factor) derived from the fits were in the range of 0.004−0.006 $Å^2$. Therefore, σ^2 was eventually fixed at the value of 0.005 $Å^2$ for all fits (thereby allowing only six parameters total to vary) to reduce scatter in the CNs, and FEFF 8.0 was used to calculate all of the other necessary parameters including the many-body amplitude reduction term S_0^2 (0.916 for Ru and 0.934 for Pt).

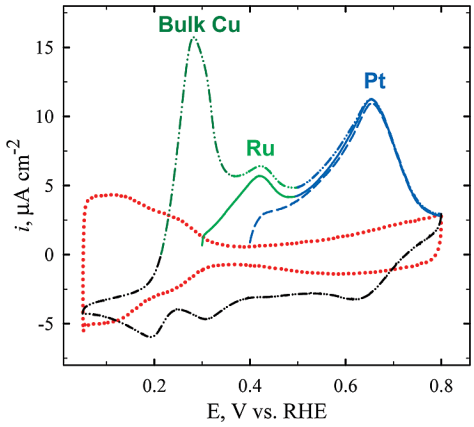

Figure 3. Cupric ion stripping voltammograms collected in 1 M TFMSA + 2 mM $CuSO_4$ taken at a sweep rate of 10 mV s^{-1}. Cyclic voltammograms of a typical PtRu black catalyst in the presence (dotted−dashed) and absence (dotted) of Cu ions showing the various underpotentially deposited regions on both Pt and Ru sites as well as the bulk Cu deposition region.

2.5. FEFF 8.0 Calculations. The FEFF 8.0 code was used to model the adsorbate $\Delta\mu$ signatures. The $\Delta\mu$(Ads) was determined by subtracting the μ-XANES of a clean "Janin" [26] type Pt_4M_2 cluster from the μ-XANES of a cluster containing an adsorbate molecule in the atop, bridged, or *n*-fold position, i.e., $\Delta\mu(O) = \mu(O/Pt_4M_2) - \mu(Pt_4M_2)$. The Janin cluster, used in much of our previous work,[34,41,48,51−56] was chosen here because it is the smallest cluster that contains atop, bridged, fcc, and hcp sites. The bond distances used in the clusters were the same as those in our previous FEFF 8.0 calculations.[48,57] In general, Pt−Pt and Pt−Ru distances used were 2.77 Å as is known from crystallographic determinations. Oxygen in the atop position was treated as OH (since the scattering from H has been shown to be indiscernible),[41,55] while oxygen in an *n*-fold position was treated as O. This is consistent with density functional theory (DFT) calculations,[26,58,59] which show that OH prefers to be singly coordinated and O doubly or triply coordinated to the Pt surface.

3. Results

3.1. Electrochemical Characterization. ***Surface Area and the Effects of Potential Cycling.*** As described above, the electrochemically active surface area for Pt and PtRu catalysts can be determined by anodically stripping the underpotential-deposited (upd) cupric ions that form a monolayer on the catalyst surface. This process is illustrated in Figure 3, which shows CVs of PtRu in the absence and presence of cupric ions. The CVs in the presence of cupric ions reveal anodic peaks which correspond to the "stripping" currents of Cu upd on the indicated surface atoms. As evident from the figure, there is a potential dependence that governs which surface atom will accept the Cu. For instance, if the potential is fixed at 0.4 V, Cu will only deposit on Pt. However, if the potential is fixed at 0.3 V, it will deposit on both the Ru and the Pt surface atoms. If the potential is cycled below 0.3 V, a bulk Cu layer is deposited and subsequently removed at 0.28 V. Cyclic voltammograms for the two PtRu materials being investigated are presented in Figure 4. The insets contain the Cu stripping curves used to calculate the electrochemically active surface area for current density normalization and surface area analysis. As evident from the figure, both materials undergo significant changes in surface area between cycles 5 and 50; the integrated results are presented in Table 1. Both materials show a decrease in the magnitude of

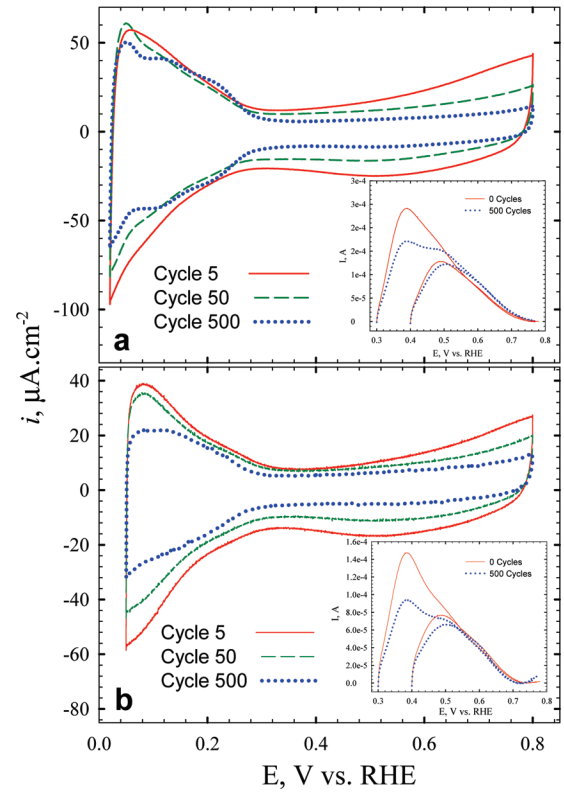

Figure 4. Cyclic voltammograms for (a) Johnson-Matthey and (b) Tanaka catalysts after 5, 50, and 500 cycles showing differences in aging properties. The actual data are the same as in ref 24 except normalized to the initial Cu stripping surface area for cycles 5 and 50 and normalized to the Cu stripping area post cycle 500 for the 500th scan. The inset shows the detail of Cu upd data for the two catalysts.

TABLE 1: Summary of Cu Stripping Results for Surface Area Analysis[a]

catalyst	cycle no.	surface metal	surface area (cm^2)	% change
JM	0	Ru	12.05	−12.0
	500	Ru	10.61	
	0	Pt	5.69	+2.74
	500	Pt	5.85	
Tanaka	0	Ru	6.91	−24.7
	500	Ru	5.20	
	0	Pt	3.40	−12.4
	500	Pt	2.98	

[a] Surface area calculations were done by integrating the Cu stripping peaks for the catalysts as described by Green et al.[38,39]

the Cu stripping off of Ru sites (*E* fixed at 0.3 V), indicating loss of surface Ru through either Ru dissolution or formation of RuO_xH_y islands as Cu ions will *not* underpotentially deposit on RuO_xH_y but only on available, free metallic Ru sites. It is worth stressing this latter point as it not only explains the Cu upd data but provides us with a mechanistic insight into the aging process, all of which will be shown to be in good agreement with results from the XAS analysis and electrochemical data. It should be noted that the Tanaka PtRu surface area loss is more than double that of JM (on both the Pt and Ru). Interestingly, the Pt surface area of the Tanaka material decreased considerably, whereas the JM Pt surface area actually increased slightly. The increase in Pt surface area for JM is likely the result of Ru dissolution from the surface of the particle unveiling newly uncovered Pt surface atoms. The loss of Pt surface area in the Tanaka sample can be attributed to either (a) Pt dissolution or (b) the formation of larger Ru islands which

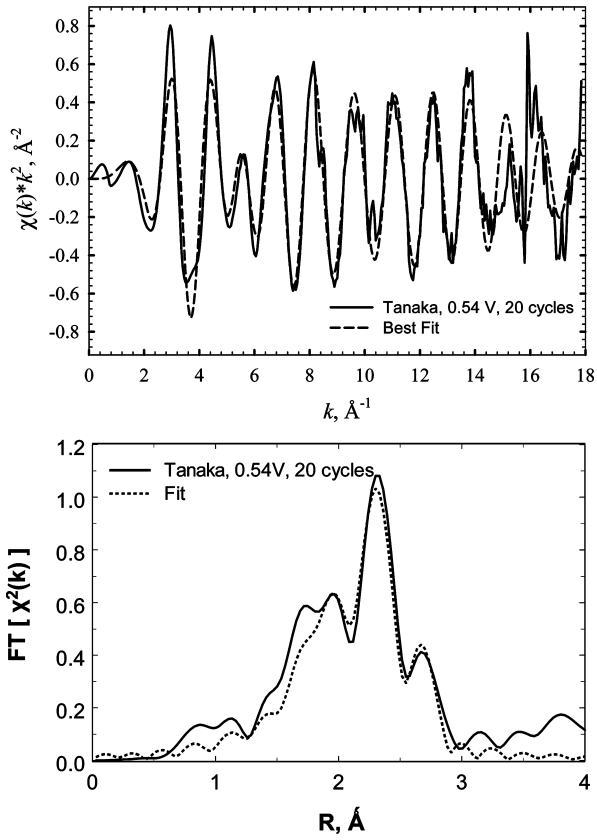

Figure 5. Representative k space (top) and Fourier-transformed (bottom) EXAFS data and fit for the Tanaka PtRu sample at the Ru K edge taken at 0.54 V after 20 cycles. The two-path (Ru−Ru and Ru−Pt) fit was performed in R space (1.574 Å$^{-1} < k <$ 13.769 Å^{-1}, k^2-weighted) and is shown with no phase correction.

mask more of the Pt surface sites. Both of the above possibilities are discussed in greater detail in the EXAFS section below.

There are also significant changes to the CV profiles illustrating particle aging as a result of potential cycling. For instance, in Figure 4 which overlays the three CVs for the JM and Tanaka PtRu samples at 5, 50, and 500 cycles, there is a very noticeable change in the H_{upd} region. At cycle 5 for the JM sample there are no discernible peaks typical of H desorption; however, as the material is cycled it develops features which are not unlike the H_{upd} region of pure Pt. The Tanaka sample, however, appears to stay more alloy-like (i.e., no discernible features). These observations may provide some information about the size of the clear Pt regions, i.e., larger in the JM case because of the smaller Ru islands. Larger regions of free Pt will more clearly resolve the H adsorption at faces and corners/edges that cause these separate features. These results are consistent with the Cu upd data above, which suggest the JM material undergoes Ru dissolution to uncover a more Pt-like surface. The Tanaka low potential region also reveals a larger decrease in H_{upd} current than that of JM, suggesting more growth in Ru(O_xH_y) coverage, consistent with the lack of Pt-like CV features. This is also consistent with the Cu stripping data and is suggestive of case b mentioned above.

3.2. EXAFS. A representative FT-EXAFS least-squares fit is shown in Figure 5 for the Ru K edge data in R space and the agreement between experiment and theory of a two-path Ru−Ru and Ru−Pt fit. Since the σ^2 values were held constant at 0.005 Å^2, this fit was actually obtained using six parameters (N, R, and E_0 for each path). Figure 6 illustrates the Ru−Ru and Ru−Pt CNs obtained from fits similar to that in Figure 5

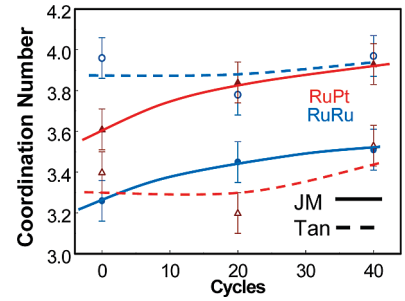

Figure 6. Changes in average Ru−Ru and Ru−Pt CNs with cycling for both the JM and Tanaka catalysts. Error bars of ±0.1 are representative of the relative error, but the absolute error is probably larger.

TABLE 2: Summary of Coordination Numbers Obtained from Pt L_{III} Edge Data[a]

sample	Pt−Pt	Pt−Ru	Pt−Pt + Pt−Ru	$\eta = 1 - N_{Pt-Ru}/N_{Ru-Pt}$
Tanaka	4.8	2.0	6.8	~0.4
JM	3.9	2.8	6.7	~0.3

[a] The relative uncertainty in CN is ca. 0.1, but the absolute uncertainty is larger.

for three different potentials, 0.0, 0.24, and 0.54 V (relatively small changes with potential were observed). The results in Figure 6 are the average of those obtained at three potentials after 0, 20, and 40 potential cycles between 0.02 and 0.8 V (2.6 min/cycle). Note that the ratio Ru−Ru/Ru−Pt is much larger for the Tanaka sample compared to the JM sample. Also, it is noticeable that the CNs increase with cycling and that this increase is much larger for the JM sample. The increase in Ru−Pt CN with cycling in the JM samples is consistent with Ru dissolution assuming the Ru with low CN at the surface preferably leaches. The increase in Ru−Ru CN suggests that the remaining Ru islands are larger, due to either Ostwald ripening or just the lower coordinated Ru leaving the surface. The CN ratio Ru−Ru/Ru−Pt reflects the Ru island size on the particle surface, since presumably the Ru in the interior of the cluster is more alloyed with Pt. Thus, the Ru islands in the Tanaka sample are significantly bigger, and therefore, little change is noticed with cycling. In contrast, the small islands on the JM catalyst undergo Ru dissolution as well as particle ripening (enlargement) with cycling.

The data in Figure 6 strongly suggest that much more Ru exists on the particle surfaces of the Tanaka samples and thus the Ru islands are larger. This is entirely consistent with the CNs obtained at the Pt edge as summarized in Table 2. Since they did not change much with cycling, we report just the average with potential and cycling (i.e., average of nine results, three potentials of three cycling levels each) in Table 3. Note that the sums of the CNs, Pt−Pt + Pt−Ru, are nearly the same, indicating nearly identical particle sizes (around 1.0−1.5 nm on the basis of spherical particles)[60] in the two samples. However, the Tanaka samples have larger Pt−Pt and smaller Pt−Ru CNs, which is consistent with more Ru existing at regions of lower coordination, i.e., at the surface.

3.3. $\Delta\mu$-XANES Analysis. To more easily understand the $\Delta\mu$-XANES data, Figure 7 shows representative (qualitative) coverages for CO and O(H) on Pt and Ru as obtained from our previous studies of three different PtRu catalysts in methanol.[61] It reveals that, at potentials below 0.3 V, the CO coverage on Pt and even on the Ru islands (the latter true only if Ru island clusters are relatively large) is nearly complete in methanol. At potentials above 0.6 V, the coverage of OH and O is nearly

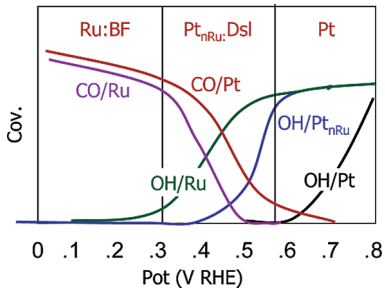

Figure 7. Representative CO and O(H) coverages for a PtRu anode in methanol as reported previously using the $\Delta\mu$-XANES technique.[61]

TABLE 3: Summary of Results from Electrochemical, Cu_{upd}, and X-ray Absorption Data

Tanaka	Johnson-Matthey
Large Ru coverage and existing as larger RuO_xH_y islands on the surface	Smaller Ru coverage and existing in highly dispersed metallic Ru islands
Islands relatively stable to Ru dissolution and growth, but the RuO_xH_y−Pt interface region grows as more Ru moves to the surface	Significant Ru dissolution and island growth and/or agglomeration with islands becoming more oxidized and leaving larger Pt open regions
CO oxidation chiefly occurs via a ligand-effect mechanism	CO oxidation chiefly occurs via a bifunctional mechanism initially but converts to a ligand-effect mechanism on aging

complete, and the CO coverage has dropped to unobservable levels. This occurs because of water activation (eq 3) and the widely accepted mechanism for CO oxidation[62−65] (eq 4).

$$H_2O + M \rightarrow OH/M + H^+ + e^- \quad (3)$$

$$CO/Pt + OH/M \rightarrow CO_2 + Pt + M \quad (4)$$

Here, M can be either surface Pt or Ru atoms, and as illustrated in Figure 7, water activation occurs at the lowest potential on Ru, followed by Pt near the Ru islands (Pt_{nRu}), and finally the Pt atoms. Figure 7 also indicates generally where the different CO oxidation mechanisms (differentiated by the source of the OH) dominate. The bifunctional mechanism (BF) dominates below 0.3 V when the facilitating OH comes from the Ru, the direct surface ligand (DsL) mechanism dominates in the range 0.3−0.5 V when the OH comes from the Pt atoms near the Ru (Pt_nRu), and the direct mechanism dominates above 0.5 V when the OH comes generally from the Pt atoms. Further, we found that large Ru islands generally are more oxidized and hence exert a larger ligand effect on the nearby Pt atoms, while smaller Ru islands experienced a "reverse" ligand effect from the Pt and were less reactive and were not oxidized at lower potentials. Therefore, the small Ru atoms were available to activate water below 0.3 V and hence carry out the BF mechanism, while the larger Ru islands were heavily oxidized, making the BF mechanism inactive. The BF mechanism is seemingly more effective when small Ru islands exist and the DsL mechanism when the larger $Ru(O_xH_y)$ islands exist. Those we term "heavily oxidized" most likely contain Ru in an oxidation state of 2−4 (as RuO_xH_y), while those termed "slightly oxidized" are

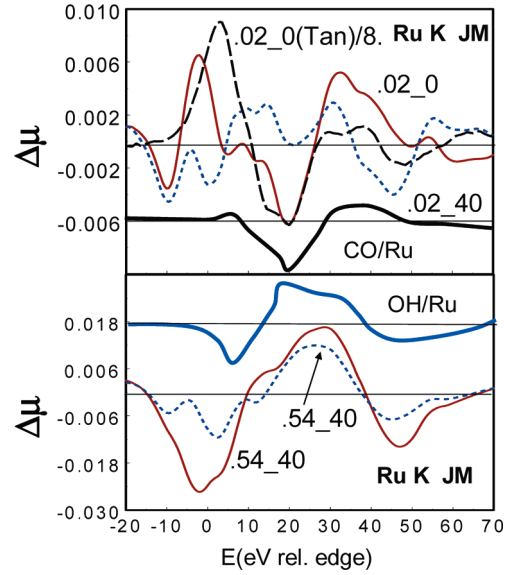

Figure 8. Comparison of $\Delta\mu(V\_cycles)$ at the Ru K edge using eq 3b. Also shown are theoretical $\Delta\mu$ signatures denoted OH/Ru and CO/Ru. Note that the $\Delta\mu$ for the Tanaka sample has been scaled by a factor of 8 to place it on the same scale.

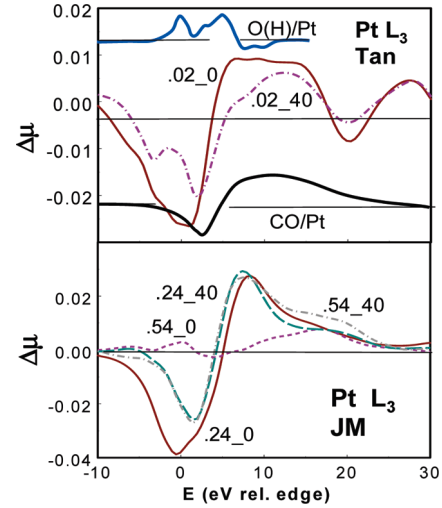

Figure 9. Comparison of $\Delta\mu(V\_cycles)$ line shapes at the Pt L_{III} edge using eq 3a. Also indicated are theoretical signatures for O(H)/Pt[27,61] and CO/Pt. The three features in the OH/Pt signature correspond to OH/Pt near a Ru site, OH/Pt away from the Ru islands, and O/Pt.

primarily metallic Ru islands and probably have a much lower oxidation state of around 0.3−1.

Figures 8 and 9 show a sampling of the $\Delta\mu$-XANES results taken at both the Ru K and Pt L_{III} edges. With 3 different potentials and 3 cycling levels at both the Ru K and Pt L_{III} edges on 2 samples, a total of 36 different $\Delta\mu$ curves were constructed; only 11 are shown in Figures 8 and 9 for clarity and to reveal the most important trends in the data. Figure 8 includes Ru K edge data using a "clean" PtRu electrode in only TFMSA at 0.02 V as the reference, i.e., obtained using eq 2, along with FEFF 8.0 calculated $\Delta\mu$ signatures[66] for CO/Ru and OH/Ru obtained as described above. The results at 0.02 V and no cycling for the Tanaka and JM samples are compared in Figure 9b. Note the division by 8 to provide comparable magnitudes for the Tanaka and JM samples. This is consistent with much more Ru at the surface in the Tanaka sample since the $\Delta\mu$ intensity primarily reflects changes at the surface, and as suggested by Figure 8, at 0.02 V the Ru islands are covered

with CO. The $\Delta\mu$ data for the Tanaka sample show a CO/Ru signature, consistent with that found previously in methanol on large Ru islands. At 0.54 V the Ru is expected to be nearly fully oxidized, and indeed, the data in Figure 8b are consistent with O(H)/Ru.

Results are also shown at the Pt L_{III} edge (Figure 9), obtained using eq 1 and compared with theoretical $\Delta\mu$ signatures obtained previously[27,61] for O(H)/Pt and CO/Pt using the procedures described above. The three peaks in the O(H)/Pt signature correspond to O(H)/Pt near Ru, O(H)/Pt, and O/Pt, respectively, enabling these species to be separately observed, and hence the representative results in Figure 7. Note that the $\Delta\mu$ curves for the Tanaka sample are much smaller, consistent with much of the Pt being covered by the large Ru islands. Thus, the EXAFS and $\Delta\mu$ data consistently reveal that the Tanaka sample has a much larger component of Ru and hence larger islands on the surface when compared with the JM samples.

4. Discussion

The results above straightforwardly show that much more Ru initially exists on the surface of the Tanaka samples compared with the JM samples, but careful comparison of the changes in $\Delta\mu$ reveals much more interesting changes with potential cycling and the nature of the Ru islands themselves. Such observations shall be discussed in greater detail in the sections that follow.

4.1. Oxidation State of Ru Islands. The ratio of the Pt−Ru/Ru−Pt CNs reflects the relative oxidation level of the Ru islands in the two samples. To understand this, consider a simple ensemble of three Pt atoms coordinated to one Ru. There will be three Pt−Ru "interactions", so the average Pt−Ru CN = 1 and Ru−Pt CN = 3 in this case; i.e., each Pt sees one Ru atom and each Ru atom three Pt atoms. Therefore, the ratio Pt−Ru/Ru−Pt (i.e., 1/3) reflects the ratio of Ru to Pt atoms. However, the catalysts contain an equal number of Pt and Ru atoms, but the oxidized Ru atoms are essentially taken out of the metal−metal scattering if they are surrounded by O atoms. Therefore, this ratio reflects the fraction of unoxidized Ru atoms and $\eta = 1 - N_{Pt-Ru}/N_{Ru-Pt}$ the fraction oxidized. These oxidized fractions are listed in Table 2. Of course, considerable Ru may exist in the interior of the particles, so this is not the total fraction of Ru at the surface that is more oxidized (those will be much higher), but these fractions are consistent with a greater fraction of Ru at the surface in the Tanaka samples. It is also worth mentioning that the larger islands are more oxidized than the smaller, more dispersed ones, which tend to be more metallic in nature, as found previously.[61] Another recent study which employed XAS (ex situ) and TEM on PtRu catalysts also provides support for the existence of oxidized Ru islands in PtRu catalysts.[67] While the *absolute size* of the islands cannot be determined by any of the methods used in this study, it is the large difference in *island size* between the highly dispersed, smaller and largely metallic Ru islands and the larger and more oxidized Ru islands that is observed and accounts for some of the differences in the aging processes occurring on the two catalysts.

The $\Delta\mu$ magnitude and signatures for the Ru islands on the Tanaka sample do not show much change with cycling, as expected for larger islands. Further, all signatures reflect CO/Ru at all potentials ≤0.54 V, consistent with Figure 7, but these larger RuO_xH_y islands exert a larger electronic or ligand effect on the nearby Pt atoms,[27,61] increasing the oxophilicity of those Pt atoms. This trend is clearly seen in Figure 9b showing some O(H)/Pt near the Ru islands already in the Tanaka samples at 0.02 V, compared with the JM sample requiring 0.54 V for this to be evident. The following sections discuss the catalyst aging process as a metal dissolution−agglomeration process increasing with the number of potential cycles and provide a visual summary of the two different aging processes as depicted in Figure 10.

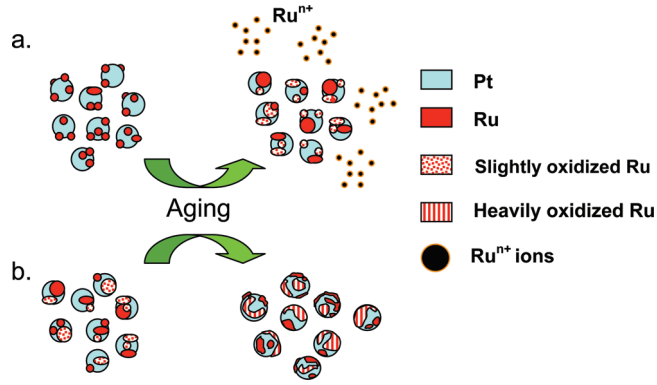

Figure 10. Schematic representation of the primary PtRu nanoparticle aging processes occurring in the (a) Johnson-Matthey and (b) Tanaka catalysts.

4.2. Ru Dissolution and Agglomeration. At 0.54 V, any Ru at the surfaces is expected to be covered with O (see Figure 7), and this is consistent with the Ru $\Delta\mu$ signatures in Figure 9b for the JM samples. However, it shows that the magnitude of this signature decreases with cycling, indicating that Ru is leaving the surface, i.e., dissolution of Ru. At 0.02 V, however, the $\Delta\mu$ signature obtained at the Ru edge reflects CO/Ru at 0 cycles, but more of an O(H) signature with a component of CO/Ru after 40 cycles. This clearly suggests that the Ru islands, as they get larger, become more oxidized as indicated above. The growth in Ru−Ru CN seen in the EXAFS can come from both particle agglomeration and Ru dissolution, since the smallest Ru islands presumably undergo dissolution the fastest. The $\Delta\mu$ data clearly show that both are occurring in the JM sample. Similar phenomena have been observed using high-resolution transmission electron microscopy (HR-TEM) and secondary ion mass spectrometry (SIMS) in a recent study on the decomposition of PtRu anode catalysts.[68]

4.3. Pt Dissolution and Agglomeration. Although not reported in Table 2, the Pt−Pt CNs in the Tanaka sample do show some variation with cycling (5.1 (0 cycles) down to 4.8 (20 cycles) and then back to 5.2 (40 cycles)). This suggests that the smaller PtRu particles initially underwent dissolution, followed by agglomeration of some of the remaining particles. The $\Delta\mu$ data are consistent with this change. The $\Delta\mu$ signatures at 0.02 V (Figure 9), when the Pt surface should be nearly covered by CO, reveal a decrease in magnitude with cycling and indeed even the presence of a small amount of OH/Pt at 0.54 V after 40 cycles. This suggests an increase in the efficiency of CO oxidation with cycling. This OH/Pt near the Ru islands is directly evident in the $\Delta\mu$(0.02_40) signature, showing the strong ligand effect of the large Ru islands in the Tanaka sample. The increase in CO oxidation (i.e., reduction in CO on the surface) with cycling either may be due to elimination of the smaller PtRu particles, where the CO oxidation might be less efficient, or at least indicates a smoothing of the Pt surface perhaps from Pt dissolution of the corners or edges. This would enable a greater fraction of more mobile CO, or more likely simply a reduction in Pt surface area consistent with the Cu upd data in Table 1. Komanicky et al.[7] found that the nanofaceted surface dissolves faster, indicating the edges and corners are the main sources of dissolution. In any event, the

extent of CO on Pt appears to decrease in magnitude with cycling for the Tanaka catalysts (Figure 9b). This is in contrast to that occurring on the JM catalysts, where Figure 9a clearly shows the opposite trend, consistent with the Cu upd data in Table 1.

4.4. Interpretation of CO Stripping Curve Changes. We can now understand the changes in the CO stripping curves for the catalysts before and after an 8 h CA test as shown earlier in Figure 1. The Ru particles on the Tanaka samples are heavily oxidized to begin with and therefore show no significant change in RuO_xH_y content on aging. There is consequently hardly any change in the onset potential for the CO oxidation as there is no change in the nature of the Ru islands. The increased CO oxidation current and peak potential are likely due to increased availability of the interface $Ru(O_xH_y)-Pt$ sites where the ligand mechanism is active, consistent with the schematic in Figure 10 showing more interface regions and less clear Pt regions. The JM sample, on the other hand, has much smaller, metallic Ru islands on the surface to begin with and, on aging, undergoes dissolution and Ru island growth via oxidation and agglomeration. The growth in island size changes the islands from mostly Ru to $Ru(O_xH_y)$, and hence, the dominant CO oxidation mechanism changes from bifunctional to the direct surface ligand effect, which moves CO oxidation to slightly higher potential as illustrated in Figure 7. It has been shown previously that available RuO_xH_y species are critical for the CO oxidation properties of a PtRu alloy catalyst.[69,70] Further, it is interesting to note that the CO stripping curves for the aged JM catalyst begin to look more like the CO stripping curves for the Tanaka catalyst. This is consistent with the fact that more of the Ru islands are now bigger and oxidized, just as the Tanaka catalysts were in their initial state prior to the aging process.

5. Conclusions

The electrochemical, EXAFS, and $\Delta\mu$-XANES analyses consistently show that the Tanaka sample has much more Ru segregated to the surface and the Ru exists in larger islands and is present in more oxidized, stable $Ru(O_xH_y)$ forms. The smaller Ru islands in the JM sample are found to undergo faster dissolution of Ru as well as agglomeration with cycling or chronoamperometric aging in methanol. The findings from this work are summarized in Table 3. These results suggest that the smaller Ru islands, which facilitate CO oxidation more favorably via the bifunctional mechanism at lower potential, are unstable in methanol at the surface of unsupported PtRu particles. Therefore, in a DMFCs, larger Ru islands, which are less susceptible to dissolution and induce a larger ligand effect (albeit at somewhat higher potential compared to that of the bifunctional mechanism) will be much more stable and effective. They also corroborate previous findings that available ruthenium oxide and hydroxide phases rather than metallic Ru along with Pt are essential for stable CO oxidation properties of a PtRu catalyst.

It could certainly be argued that, with the proposed aging mechanisms evident in this work, the JM particles should eventually become more like the Tanaka catalysts, consistent with the CO oxidation curves in Figure 1. However, the CVs in Figure 4 suggest that there are still significant differences after cycling. It is thus apparent that, in the case of the JM catalysts, while some of the smaller Ru particles are lost to dissolution and others grow in size on the surface due to Ostwald ripening and agglomeration, the islands are still a bit smaller and hence less oxidized compared with those found on the Tanaka catalysts. The XAS and CO stripping results above show that the Tanaka sample in comparison with the JM catalyst actually showed some signs of improvement after 40 cycles, consistent with some RuO_xH_y island growth even in the Tanaka catalysts.

Acknowledgment. Financial support for this project was provided by the Army Research Office via both Single Investigator and Multi University Research Initiatives (P.I. Case Western Reserve University). We are also grateful for the use of beamline X23-A2 at the National Synchrotron Light Source, Brookhaven National Laboratory, which is supported by the U.S. Department of Energy, Office of Science, Office of Basic Energy Sciences, under Contract No. DE-AC02-98CH10886. We also thank Tanaka Kikinzoku International for supplying their PtRu catalyst at no cost.

References and Notes

(1) *Fuel Cells Durability and Performance: Stationary, Automotive, Portable*, 1st ed.; William Andrew Applied Science Publishers: Norwich, NJ, 2006; p 400.
(2) Borup, R.; Davey, J.; Wood, D.; Garzon, F.; Inbody, M. *PEM Fuel Cell Durability*; DOE Hydrogen Program Progress Report; U.S. Department of Energy: Washington, DC, 2005.
(3) Dam, V. A.; de Bruijn, F. *J. Elecrochem. Soc.* **2007**, *154*, B495.
(4) Ferreira, P. J.; la O', G. J.; Shao-Horn, Y.; Morgan, D.; Makharia, R.; Kocha, S.; Gasteiger, H. A. *J. Electrochem. Soc.* **2005**, *152*, A2256.
(5) Johnson, D. C.; Napp, D. T.; Bruckenstein, S. *Electrochim. Acta* **1970**, *15*, 1493.
(6) Kinoshita, K.; Lundquist, J. T.; Stonehart, P. *J. Electroanal. Chem.* **1973**, *48*, 157.
(7) Komanicky, V.; Chang, K. C.; Menzel, A.; Markovic, N. M.; You, H.; Wang, X.; Myers, D. *J. Electrochem. Soc.* **2006**, *53*, B446.
(8) Ota, K.; Nishigori, S.; Kamiya, N. *J. Electroanal. Chem.* **1988**, *247*, 205.
(9) Ralph, T. R.; Hogarth, M. P. *Platinum Met. Rev.* **2002**, *46*, 117.
(10) Rand, D. A. J.; Woods, R. *J. Electroanal. Chem.* **1972**, *36*, 57.
(11) Wang, X.; Kumar, R.; Myers, D. J. *Electrochem. Solid-State Lett.* **2006**, *9*, A225.
(12) Wilson, M. S.; Garzon, F.; Sickafus, K. E.; Gottesfeld, S. *J. Electrochem. Soc.* **1993**, *140*, 2872.
(13) Xie, J.; Wood, D. L.; More, K. L.; Atanassov, P.; Borup, R. L. *J. Electrochem. Soc.* **2005**, *152*, A104.
(14) Yasuda, K.; Taniguchi, A.; Akita, T.; Ioroi, T.; Siroma, Z. *Phys. Chem. Chem. Phys.* **2006**, *8*, 746.
(15) Antolini, E.; Salgado, J. R. C.; Gonzalez, E. R. *J. Power Sources* **2006**, *160*, 957.
(16) Chen, W.; Sun, G.; Liang, Z.; Mao, Q.; Li, H.; Wang, G.; Xin, Q.; Chang, H.; Pak, C.; Seung, D. *J. Power Sources* **2006**, *160*, 933.
(17) Holstein, W. L.; Rosenfeld, H. D. *J. Phys. Chem. B* **2005**, *109*, 2176.
(18) Hwang, B. J.; Sarma, L. S.; Chen, J. M.; Chen, C. H.; Shih, S. C.; Wang, G. R.; Liu, D. G.; Lee, J. F.; Tang, M. T. *J. Am. Chem. Soc.* **2005**, *127*, 11140.
(19) Jeon, M. K.; Lee, K. R.; Oh, K. S.; Hong, D. S.; Won, J. Y.; Li, S.; Woo, S. I. *J. Power Sources* **2006**, *158*, 1344.
(20) Liu, J.; Zhou, Z.; Zhao, X.; Q., X.; G, S.; B., Y. *Phys. Chem. Chem. Phys.* **2004**, *6*, 134.
(21) Lukaszewski, M.; Czerwinski, A. *J. Electroanal. Chem.* **2006**, *589*, 38.
(22) Sarma, L. S.; Chen, C. H.; Wang, G. R.; Hsueh, K. L.; Huang, C. P.; Sheu, H. S.; Liu, D. G.; Lee, J. F.; Hwang, B. J. *J. Power Sources* **2007**, *167*, 358.
(23) Christian, E.; Piotr, P.; John, D.; Piotr, Z. *J. Electrochem. Soc.* **2006**, *153*, A171.
(24) Gancs, L.; Hakim, N.; Hult, B.; Mukerjee, S. *ECS Trans.* **2006**, *3*, 607.
(25) Piela, P.; Eickes, C.; Brosha, E.; Garzon, F.; Zelenay, P. *J. Elecrochem. Soc.* **2004**, *151*, A2053.
(26) Janin, E.; von Schenck, H.; Gothelid, M.; Karlsson, U. O.; Svensson, M. *Phys. Rev. B* **2000**, *61*, 13144.
(27) Scott, F. J.; Roth, C.; Ramaker, D. E. *J. Phys. Chem. C* **2007**, *111*, 11403.
(28) Murthi, V.; Arruda, T.; Gancs, L.; Shyam, B.; Ramaker, D.; Mukerjee, S. *Meet. Abstr.—Electrochem. Soc.* **2007**, *702*, 403.
(29) Darling, R. M.; Meyers, J. P. *J. Elecrochem. Soc.* **2003**, *150*, A1523.
(30) Anderson, A. B.; Shiller, P. *J. Phys. Chem. B* **1998**, *102*, 2696.
(31) Wang, Z.-B.; Rivera, H.; Wang, X.-P.; Zhang, H.-X.; Feng, P.-X.; Lewis, E. A.; Smotkin, E. S. *J. Power Sources* **2008**, *177*, 386.

(32) Wang, Z.-B.; Wang, X.-P.; Zuo, P.-J.; Yang, B.-Q.; Yin, G.-P.; Feng, X.-P. *J. Power Sources* **2008**, *181*, 93.
(33) Zhang, J.; Sasaki, K.; Sutter, E.; Adzic, R. R. *Science* **2007**, *315*, 220.
(34) Ramaker, D. E.; Koningsberger, D. C. *Phys. Rev. Lett.* **2002**, *89*, 139701.
(35) McBreen, J.; Mukerjee, S. *J. Elecrochem. Soc.* **1995**, *142*, 3399.
(36) McBreen, J.; O'Grady, W. E.; Pandya, K. I.; Hoffman, R. W.; Sayers, D. E. *Langmuir* **1987**, *3*, 428.
(37) Enayetullah, M. A.; DeVilbiss, T. D.; Bockris, J. O. *J. Electrochem. Soc.* **1989**, *136*, 3369.
(38) Green, C. L.; Kucernak, A. *J. Phys. Chem. B* **2002**, *106*, 1036.
(39) Green, C. L.; Kucernak, A. *J. Phys. Chem. B* **2002**, *106*, 11446.
(40) Koningsberger, D. C.; de Graaf, J.; Mojet, B. L.; Ramaker, D. E.; Miller, J. T. *Appl. Catal., A* **2000**, *191*, 205.
(41) Teliska, M.; O'Grady, W. E.; Ramaker, D. E. *J. Phys. Chem. B* **2005**, *108*, 2333.
(42) Ramaker, D. E.; Mojet, B. L.; Garriga Oostenbrink, M. T.; Miller, J. T.; Koningsberger, D. C. *Phys. Chem. Chem. Phys.* **1999**, *1*, 2293.
(43) Koningsberger, D. C.; de Graaf, J.; Mojet, B. L.; Ramaker, D. E.; Miller, J. T. *Appl. Catal., A* **2000**, *191*, 205.
(44) Arruda, T. M.; Shyam, B.; Ziegelbauer, J. M.; Mukerjee, S.; Ramaker, D. E. *J. Phys. Chem. C* **2008**, *112*, 18087.
(45) Teliska, M.; O'Grady, W. E.; Ramaker, D. E. *J. Phys. Chem. B* **2004**, *108*, 2333.
(46) Teliska, M.; O'Grady, W. E.; Ramaker, D. E. *J. Phys. Chem. B* **2005**, *109*, 8076.
(47) Teliska, M.; Murthi, V. S.; Mukerjee, S.; Ramaker, D. E. *J. Elecrochem. Soc.* **2005**, *152*, A2159.
(48) Scott, F. J.; Mukerjee, S.; Ramaker, D. E. *J. Electrochem. Soc.* **2007**, *154*, A396.
(49) Ravel, B.; Newville, M. *J. Synchrotron Radiat.* **2005**, *12*, 537.
(50) Newville, M.; Livins, P.; Yacoby, Y.; Rehr, J. J.; Stern, E. A. *Phys. Rev. B* **1993**, *47*, 14126.
(51) Koningsberger, D. C.; de Graaf, J.; Mojet, B. L.; Ramaker, D. E.; Miller, J. T. *J. Catal., A* **2000**, *191*, 205.
(52) Koningsberger, D. C.; Oudenhuijzen, M. K.; Bitter, J. H.; Ramaker, D. E. *Top. Catal.* **2000**, *10*, 167.
(53) Mojet, B. L.; Miller, J. T.; Ramaker, D. E.; Koningsberger, D. C. *J. Catal.* **1999**, *186*, 373.
(54) Mojet, B. L.; Ramaker, D. E.; Miller, J. T.; Koningsberger, D. C. *Catal. Lett.* **1999**, *62*, 15.
(55) Ramaker, D. E.; Mojet, B. L.; Oostenbrink, G.; Miller, J. T.; Koningsberger, D. C. *Phys. Chem. Chem. Phys.* **1999**, *1*, 2293.
(56) Teliska, M.; Murthi, V. S.; Mukerjee, S.; Ramaker, D. E. *J. Phys. Chem. C* **2007**, *111*, 9267.
(57) Scott, F. J.; Roth, C.; Ramaker, D. E. *J. Phys. Chem. C*, in press.
(58) Balbuena, P. B.; Altomare, D.; Vadlamani, N.; Bingi, S.; Agapito, L. A.; Seminario, J. M. *J. Phys. Chem. A* **2004**, *108*, 6378.
(59) Xu, Y.; Ruban, A. V.; Mavrikakis, M. *J. Am. Chem. Soc.* **2004**, *126*, 4717.
(60) Hardeveld R.V., M. A. V. *Surf. Sci.* **1969**, *4*, 396.
(61) Scott, F. J.; Mukerjee, S.; Ramaker, D. E. *J. Electrochem. Soc.* **2007**, *154*, A396.
(62) M. Watanabe, S. M. *J. Electroanal. Chem.* **1975**, *60*, 275.
(63) Ticanelli, E.; Beery, J. G.; Paffett, M. T.; Gottesfeld, S. *J. Electroanal. Chem.* **1989**, *258*, 61.
(64) Kim, H.; Rabelo de Moraes, I.; Tremiliosi-Filho, G.; Haasch, R.; Wieckowski, A. *Surf. Sci.* **2001**, *474*, L203.
(65) Davies, J. C.; Hayden, B. E.; Pegg, D. J. *Surf. Sci.* **2000**, *467*, 118.
(66) Ankudinov, A. L.; Ravel, B.; Rehr, J. J.; Conradson, S. D. *Phys. Rev. Lett.* **1998**, *B58*, 7565.
(67) Nitani, H.; Nakagawa, T.; Daimon, H.; Kurobe, Y.; Ono, T.; Honda, Y.; Koizumi, A.; Seino, S.; Yamamoto, T. A. *Appl. Catal., A* **2007**, *326*, 194.
(68) Park, G.-S.; Pak, C.; Chung, Y.-S.; Kim, J.-R.; Jeon, W. S.; Lee, Y.-H.; Kim, K.; Chang, H.; Seung, D. *J. Power Sources* **2008**, *176*, 484.
(69) Long, J. W.; Stroud, R. M.; Swider-Lyons, K. E.; Rolison, D. R. *J. Phys. Chem. B* **2000**, *104*, 9772.
(70) Vijayaraghavan, G.; Gao, L.; Korzeniewski, C. *Langmuir* **2003**, *19*, 2333.

JP905383N